PLASMONIC CHEMISTRY

Driving energetically unfavorable dehydrogenation dynamics with plasmonics

Katherine Sytwu[1], Michal Vadai[2], Fariah Hayee[3], Daniel K. Angell[2], Alan Dai[4], Jefferson Dixon[5], Jennifer A. Dionne[2]*

Nanoparticle surface structure and geometry generally dictate where chemical transformations occur, with higher chemical activity at sites with lower activation energies. Here, we show how optical excitation of plasmons enables spatially modified phase transformations, activating otherwise energetically unfavorable sites. We have designed a crossed-bar Au-PdH_x antenna-reactor system that localizes electromagnetic enhancement away from the innately reactive PdH_x nanorod tips. Using optically coupled in situ environmental transmission electron microscopy, we track the dehydrogenation of individual antenna-reactor pairs with varying optical illumination intensity, wavelength, and hydrogen pressure. Our in situ experiments show that plasmons enable new catalytic sites, including dehydrogenation at the nanorod faces. Molecular dynamics simulations confirm that these new nucleation sites are energetically unfavorable in equilibrium and only accessible through tailored plasmonic excitation.

Nanoparticle (NP) phase transformations and their transient states underlie many technologies in energy storage, memory, and catalysis (*1*–*3*). These intermediate states support distinct electronic and material configurations from equilibrium that have enabled novel reaction pathways for alloying and chemical reactions (*4*, *5*). However, modifying these phase transformation dynamics requires bridging the length-scale gap between the atomic-scale structural features (i.e., atomic coordination number, surface strain, etc.) that influence dynamics and the macroscale extrinsic parameters (i.e., temperature, chemical environment, etc.) that can be controlled.

Optical excitation of localized surface plasmon resonances (LSPRs) offers a solution for overcoming this size mismatch. LSPRs create regions of high electromagnetic field intensity, or electromagnetic (EM) "hotspots," which underpin increased chemical kinetics seen in plasmon photocatalysis and plasmon-driven NP growth (*6*–*8*). LSPRs can also modify electronic and molecular energy levels and enable access to excited-state dynamics, opening new reaction pathways that are difficult or impossible to achieve under typical conditions (*9*). As the spatial distribution of EM hotspots is determined by NP geometry, LSPRs could provide the required nanoscale spatial control over transient states, reshaping the energy landscape of reactants, intermediates, and products (*10*).

Here, we provide a proof-of-concept demonstration that LSPRs can enable new transient states in NP transformations, specifically the dehydrogenation of palladium hydride (PdH_x) from its hydrogen-rich β-phase ($x \sim 0.6$) to a hydrogen-poor α-phase ($x \sim 0.01$). Our system concentrates EM enhancement at a site where chemical activity is inherently less favored, showing that LSPRs can transform a normally nonreactive NP surface facet into the preferred reaction site, in contrast to other studies in which the regions of plasmonic enhancement overlap with regions of high innate chemical activity. By exploring this intersection, we show how chemical hotspots can be tuned to coincide with the optical EM hotspot (*10*).

To demonstrate this result, it is crucial to simultaneously achieve sufficient spatial information to resolve NP features, temporal resolution to identify transient events, and chemical information to distinguish material transformations. Techniques such as super-resolution chemical imaging (*11*), ex situ NP markers (*6*), and environmental electron spectroscopy (*7*) have pushed toward simultaneous recording of spatial, temporal, and chemical information with high resolution at the nanoscale. We used optically coupled environmental transmission electron microscopy (TEM) (*12*) (Fig. 1A) to track the phase transition in situ in individual NPs with ~100-ms temporal resolution under various illumination conditions and gas pressures.

The dehydrogenation phase transition is controlled by the surrounding temperature and chemical potential (i.e., H_2 pressure) and at 246 K is endothermic (enthalpy change $\Delta H > 0$) and nonspontaneous (free energy change $\Delta G \gg k_B T$, where k_B is the Boltzmann constant and T is temperature). We used light to excite LSPRs to overcome the energetic activation barrier from the thermodynamically stable β-phase to the metastable α-phase (Fig. 1B). Experimental studies have reported this activation barrier to span from 20 to 80 kJ/mol H (0.2 to 0.8 eV) (*13*, *14*), which can be readily overcome by visible-frequency photons.

The plasmonic antenna-reactor structure consisted of a 60- to 90-nm-wide plasmonic Au nanobar antenna surrounded by a thin 2-nm SiO_2 spacer layer and a PdH_x nanorod crossed on top. This geometry spatially separated the EM hotspots from the favorable nucleation sites at the NP tips (*15*, *16*). The Au nanobars are lithographically patterned onto a Si_3N_4 TEM grid and support a transverse-mode dipolar LSPR whose resonant wavelength ranges from 600 to 680 nm with varying nanobar width, as seen in the dark-field optical images and spectra in Fig. 1C and verified with simulations (fig. S5). Next, colloidally synthesized pentatwinned Pd nanorods 350 to 550 nm in length were drop-cast onto the prefabricated TEM grid, and the crossed geometry was randomly formed (Fig. 1D). Cathodoluminescence (CL) spectra of the structure with the drop-cast Pd NPs (Fig. 1C) revealed a broad shoulder from 400 to 600 nm originating from the Si_3N_4 substrate and a LSPR peak in agreement with the dark-field optical spectra. A slight shift in the LSPR peak for the 60-nm-wide Au nanobars was caused by electron beam–induced radiative defects in the SiO_2 (fig. S7). At the crossing junction, the transverse dipolar LSPR mode transformed into a gap LSPR mode, resulting in EM hotspots localized in the gap between the Pd nanorod and Au nanobar (Fig. 1E).

To track the dehydrogenation, we used displaced-aperture dark-field (DADF) imaging to exploit the 2 to 3% decrease in lattice parameter as the NP transformed from the β- to the α-phase (*17*). After setting the temperature and hydrogen pressure such that the NP was stable in the hydrogenated β-phase (see methods), we placed an objective aperture around a diffraction point of the PdH_x nanorod (Fig. 2A) to obtain a dark-field image of the bottom PdH_x nanorod crystallite (Fig. 2B, top). Upon transformation to the α-phase, the lattice shrinks and shifts the diffraction point outside the aperture such that the DADF image could not be formed (Fig. 2B, bottom). We used this presence or absence of the DADF image as a real-time proxy for the NP hydrogenation state.

By continually dropping the hydrogen pressure (see methods), we tracked the natural dehydrogenation pathway of an isolated PdH_x nanorod (Fig. 2C). The DADF images showed the right nanorod tip transforming into α-phase, and then a second nucleation from the opposite tip after 35 s, until the NP was fully transformed

[1]Department of Applied Physics, Stanford University, 348 Via Pueblo, Stanford, CA 94305, USA. [2]Department of Materials Science and Engineering, Stanford University, 496 Lomita Mall, Stanford, CA 94305, USA. [3]Department of Electrical Engineering, Stanford University, 350 Jane Stanford Way, Stanford, CA 94305, USA. [4]Department of Chemical Engineering, Stanford University, 443 Via Ortega, Stanford, CA 94305, USA. [5]Department of Mechanical Engineering, Stanford University, 440 Escondido Mall, Stanford, CA 94305, USA.
*Corresponding author. Email: jdionne@stanford.edu

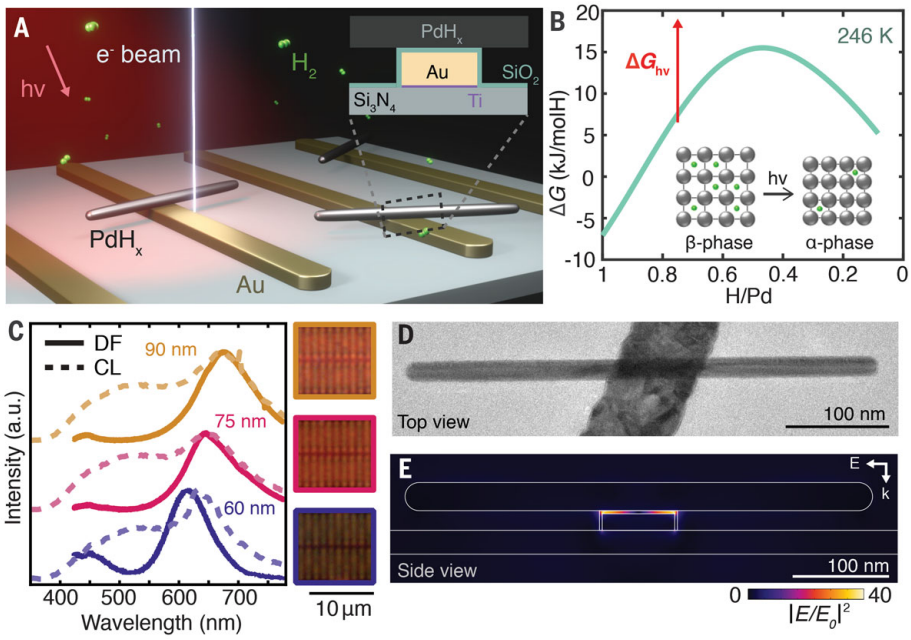

Fig. 1. The plasmonic Au-PdH_x crossed-bar nanostructure. (**A**) Schematic of the experiment in real space, with the inset showing a cross-sectional view of the intersection between the Au nanobar and PdH_x nanorod. (**B**) Schematic of the experiment in energy space, showing the Gibbs free energy of formation for PdH_x at 246 K, calculated using a mean-field lattice gas model with finite size corrections (see methods) and the excited plasmon overcoming the energy barrier. (**C**) Dark-field optical (DF) and cathodoluminescence (CL) spectra of SiO_2-coated Au nanobars of varying width (60 to 90 nm) and their corresponding dark-field optical images (right). The CL spectra are of the structure with Pd NPs scattered on top. a.u., arbitrary units. (**D**) TEM image showing a top-down view of a single Au-Pd crossed-bar nanoparticle system. (**E**) Cross-sectional view of the simulated electromagnetic enhancement of the Au-Pd system on resonance under transverse excitation. E is the electric field polarization direction, and k is the wave vector.

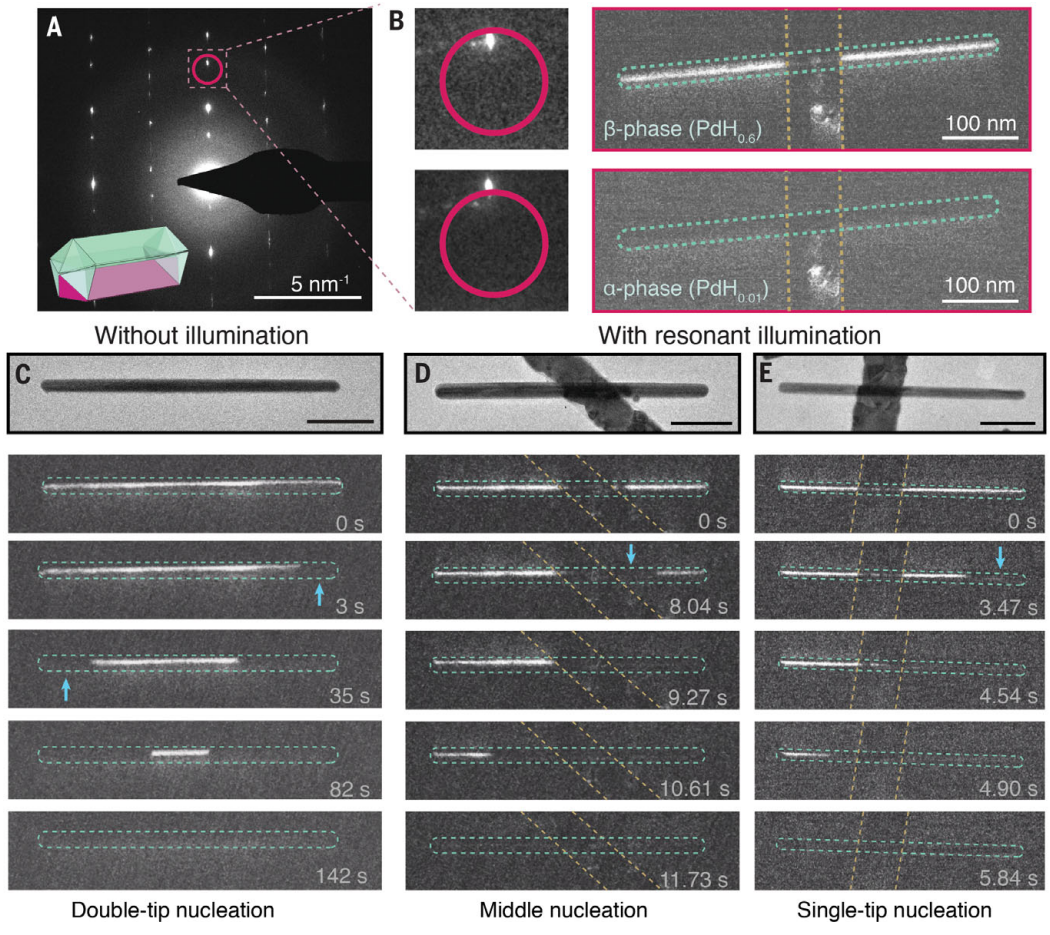

Fig. 2. Live displaced-aperture dark-field (DADF) imaging of the PdH_x dissociation dynamics. (**A**) Electron diffraction pattern of a pentatwinned PdH_x nanorod. The pink circle designates the approximate location of the objective aperture around the (220) diffraction point for DADF imaging, with inset schematic highlighting the corresponding bottom crystallite. (**B**) Zoom-in of the diffraction points relative to the actual position of the objective aperture (pink) and corresponding DADF image of the nanorod in β-phase (top) and α-phase (bottom). (**C**) TEM image and DADF snapshots of the dehydrogenation mechanism of a 498-nm PdH_x nanorod without illumination, with blue arrows indicating nucleation sites. Time labels refer to the time from the first nucleation event. See fig. S6 for more examples. (**D** and **E**) TEM and DADF snapshots of the dehydrogenation mechanism of the Au-PdH_x system under resonant illumination [(D) 627 nm with 50-nm bandwidth and (E) 640 nm with 20-nm bandwidth] for (D) a 446-nm nanorod at 75 Pa of H_2 gas and (E) a 447-nm nanorod at 70 Pa of H_2 gas. Time labels refer to the time from the start of illumination. Aqua and yellow dashed lines serve as guides-to-the-eye of nanoparticle boundaries. All scale bars are 100 nm.

into the α-phase. In eight measurements of five isolated PdH_x nanorods, we exclusively observed nucleation of the α-phase growing from both ends of the NP, herein referred to as double-tip nucleation. Our prior measurements of the thermodynamic hydrogenation behavior of long nanorods showed that Pd nanorods at these lengths (>350 nm) were more likely to nucleate their new phase at both tips (*16*). Not only were the tips the active site for our dissolution process, but PdH_x nanorods of this length energetically preferred two nucleation sites.

The addition of plasmonic hotspots modified the dehydrogenation behavior. We set the H_2 partial pressure such that the nanorods were kinetically trapped in the β-phase. Using a tunable pulsed laser, we illuminated the sample near its resonant wavelength and tracked the response of a single crossed-bar system. For some nanorods, the middle section of the PdH_x nanorod, near the EM hotspot, dehydrogenated first (Fig. 2D), showing one phase front propagating toward the nearest nanorod tip, followed by the opposite phase front propagating toward the other end. We also observed nanorods that upon illumination dehydrogenated exclusively from one of the tips (Fig. 2E) but, unlike the dark condition, did not have a second nucleation event at the opposite tip.

This single-tip nucleation was not spatially correlated with the EM hotspot, suggesting that the optical hotspot was not the sole determinant of where a reaction happens. Given the differences in experimental setup, the kinetics with and without illumination cannot be quantitatively compared, but we note that the plasmon-driven dehydrogenation process was faster, in agreement with our prior observations of PdH_x nanocubes (*12*). Furthermore, upon turning illumination off, some observed particles immediately switched back to β-phase, indicating that this phase transition is indeed driven by the optical illumination rather than only electron-beam excitation (fig. S8).

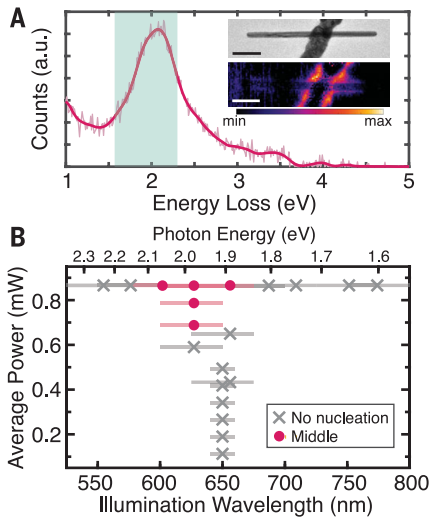

Fig. 3. Illumination dependence of nucleation site. (**A**) Electron energy loss spectra of the LSPR mode (pink is smoothed spectra), with the corresponding TEM image and EELS map of the NP (top and bottom inset, respectively). Aqua shaded region indicates the illumination range in the nucleation site experiments in (B). All scale bars are 100 nm. (**B**) Nucleation site of the α-phase for various illumination wavelengths and powers on the Au-PdH_x pair in (A) in 77 Pa of H_2 gas. Bars show the illumination bandwidth.

Wavelength-dependent studies verified that this process was driven by optically excited plasmons. We tracked the nucleation site in two individual Au-PdH_x pairs as a function of illumination wavelength and power to confirm LSPR dependence. By comparing electron energy loss spectroscopy (EELS) measurements with wavelength-dependent nucleation dynamics of the same nanobar system, we found that middle nucleation only occurs for illumination wavelengths that overlap with the LSPR of the crossed-bar structure. For example, in Fig. 3A, the LSPR mode peaked at 2.07 eV (599 nm), and its corresponding EELS map verified its transverse LSPR origin. When the system was then illuminated, the nanorod only underwent middle nucleation for illumination from 575 to 675 nm, that is, near the LSPR peak (Fig. 3B). This result was also consistent with the faster reaction times observed under 600-nm center illumination (fig. S11).

Illumination at higher photon energies but the same power did not induce middle nucleation, confirming that resonance conditions are needed and that the phase transition was not mainly driven by an absorption process (i.e., the radiative defect in SiO_2, laser heating, etc.). Likewise, at lower illumination powers, we did not observe nucleation of the dehydrogenated phase at the resonant illumination wavelength, suggesting a threshold power to induce the phase transition. The possibility of a threshold power is further supported by the observation of off-resonant illumination initiating a phase transition at higher powers than on-resonant illumination (fig. S12).

This plasmon-induced behavior not only depended on the LSPR characteristics but also the thermodynamic state of the PdH_x nanorod, indicated by the surrounding hydrogen pressure. To isolate the role of inherent thermodynamics, we tracked the nucleation site in 22 Au-PdH_x pairs under constant resonant illumination but at various H_2 pressures, six of which are highlighted in Fig. 4A (additional statistics are shown in fig. S14). As individual NPs had different dehydrogenation pressures and illumination intensities (fig. S13 and table S2), we can only quantitatively compare across a single Au-PdH_x pair, not across NPs.

Under illumination, we observed five different phase transition mechanisms: no phase transition, single-tip nucleation (15 NPs), double-tip nucleation (one NP), middle nucleation (nine NPs), and defect nucleation (one NP) (the statistics are summarized in Fig. 4B). Many NPs showed different dehydrogenation mechanisms depending on the surrounding hydrogen pressure. Consistently, when the PdH_x nanorod was very stable in its β-phase (higher H_2 pressure), the energetic barrier to nucleate a phase transition was too high, and we either observed no dehydrogenation within our data acquisition period (180 s) or a more energetically favorable mechanism such as single-tip nucleation. However, once the pressure was lowered to near the natural dehydrogenation pressure, we started to see both middle and single-tip nucleation.

We hypothesized that plasmons not only supplied the system with enough energy to undergo a less favorable transition, but careful tailoring of the conditions also allowed for new transition mechanisms such as middle nucleation. To verify this hypothesis, we qualitatively compared the energies of our three nucleation configurations using molecular dynamics simulations. We calculated the ΔG of three nanobars with identical β-phase volume fractions but different spatial configurations, simulating double-tip, single-tip, and middle nucleation, and compared it against that of a fully hydrogenated nanobar, or our starting configuration (Fig. 4C). For all nanobar lengths, we found that double-tip nucleation was the closest in energy to the fully hydrogenated nanobar, whereas middle nucleation had the largest energy difference. Single-tip and middle nucleation are close in energy, suggesting why both single-tip and middle nucleation are observed in near-equal probabilities under resonant illumination.

The LSPR decay products of light, hot carriers, and heat can all induce dehydrogenation and reduce the nucleation energy barrier. Increased radiation at the EM hotspot can locally reduce the energy barrier for hydrogen recombination and desorption, allowing hot carriers to populate the necessary Pd-H orbitals (*18*), as previously demonstrated with PdH_x cubes (*12*). The hot carriers' short lifetime (tens of femtoseconds) and mean free path [~40 nm for Au and between 10 and 20 nm for PdH_x (*19*)] imply that their spatial distribution should also follow the localized profile of the EM enhancement. The thermal distribution, however, initially follows the spatial profile of the EM enhancement but then spatially broadens over time owing to nanoscale heat transfer (fig. S15).

Therefore, activity far away from the EM hotspot could only be induced by plasmonic heating and is likely the dominant mechanism for single-tip nucleation. The overall

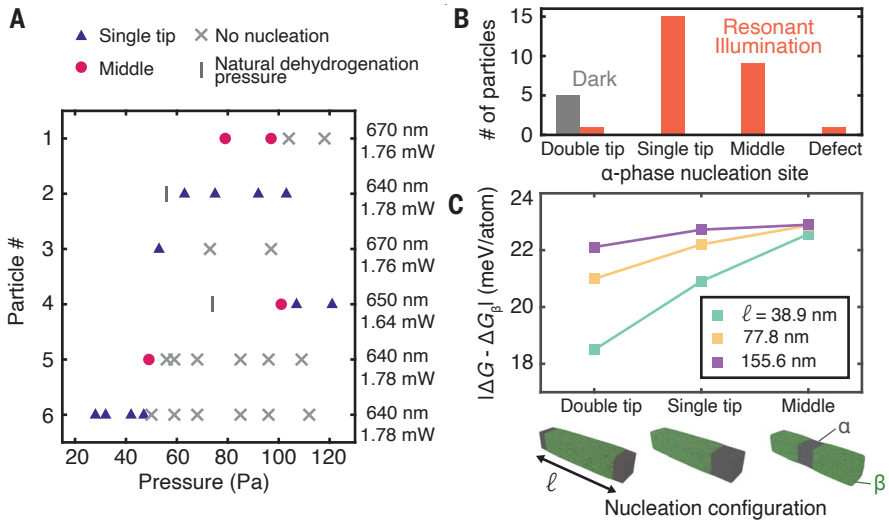

Fig. 4. Different dehydrogenation configurations of the PdH_x nanorod. (**A**) Pressure-dependent nucleation behavior for six different Au-PdH_x pairs under resonant illumination (with average illumination wavelength and power specified in the right column). (**B**) Particle statistics of α-phase nucleation site under dark and resonant illumination conditions for five NPs under dark conditions and 21 particles under illumination conditions. Some particles are counted twice because they show different responses, depending on the surrounding hydrogen pressure. (**C**) The difference in free energy between three different nucleation configurations and a fully hydrogenated nanobar (ΔG_β), calculated via MD simulations of 20-nm-width and 38.9- (aqua), 77.8- (yellow), and 155.6-nm-length (purple) nanobars.

increased temperature allowed the PdH_x nanorod to transform from the otherwise stable β-phase into α-phase but without preferential bias toward the EM hotspot. Our pressure-dependent measurements (specifically particle 4 in Fig. 4A) show single-tip nucleation at high pressures but middle nucleation at lower pressures despite identical illumination conditions. Assuming that the slight difference of 6 Pa has minimal effects on heat dissipation, then these two nucleation events had comparable heat profiles. Thus, we hypothesize that middle nucleation is primarily caused by a combination of EM enhancement and hot carriers.

REFERENCES AND NOTES

1. Y. Liu, G. Zhou, K. Liu, Y. Cui, *Acc. Chem. Res.* **50**, 2895–2905 (2017).
2. M. Wuttig, H. Bhaskaran, T. Taubner, *Nat. Photonics* **11**, 465–476 (2017).
3. F. F. Tao, P. A. Crozier, *Chem. Rev.* **116**, 3487–3539 (2016).
4. Y. Niu *et al.*, *Angew. Chem. Int. Ed.* **58**, 4232–4237 (2019).
5. X. Zhang *et al.*, *Nat. Catal.* **3**, 411–417 (2020).
6. E. Cortés *et al.*, *Nat. Commun.* **8**, 14880 (2017).
7. W. D. Yang *et al.*, *Nat. Mater.* **18**, 614–619 (2019).
8. H. Fujiwara, T. Suzuki, C. Pin, K. Sasaki, *Nano Lett.* **20**, 389–394 (2020).
9. L. Zhou *et al.*, *Science* **362**, 69–72 (2018).
10. J. Gargiulo, R. Berté, Y. Li, S. A. Maier, E. Cortés, *Acc. Chem. Res.* **52**, 2525–2535 (2019).
11. N. Zou *et al.*, *ACS Nano* **12**, 5570–5579 (2018).
12. M. Vadai, D. K. Angell, F. Hayee, K. Sytwu, J. A. Dionne, *Nat. Commun.* **9**, 4658 (2018).
13. A. Stolaś, I. Darmadi, F. A. A. Nugroho, K. Moth-Poulsen, C. Langhammer, *ACS Appl. Nano Mater.* **3**, 2647–2653 (2020).
14. T. B. Flanagan, W. Luo, J. D. Clewley, *J. Less Common Met.* **172–174**, 42–55 (1991).
15. K. Sytwu *et al.*, *Nano Lett.* **18**, 5357–5363 (2018).
16. F. Hayee *et al.*, *Nat. Commun.* **9**, 1775 (2018).
17. T. Yokosawa, T. Alan, G. Pandraud, B. Dam, H. Zandbergen, *Ultramicroscopy* **112**, 47–52 (2012).
18. V. A. Spata, E. A. Carter, *ACS Nano* **12**, 3512–3522 (2018).
19. W. E. Vargas, I. Rojas, D. E. Azofeifa, N. Clark, *Thin Solid Films* **496**, 189–196 (2006).

ACKNOWLEDGMENTS

The authors acknowledge D. Swearer for helpful discussions, R. Kim for TEM assistance, and all members of the Dionne group for helpful scientific feedback and support. **Funding:** We gratefully acknowledge funding support from C.-C. Kao at SLAC National Accelerator Laboratory; the National Science Foundation's Alan T. Waterman Award; and the U.S. Department of Energy, Office of Science, Division of Materials Science and Engineering under contract DE-AC02-76SF00515. Part of this work was performed at the Stanford Nanofabrication Facility (SNF) and Stanford Nano Shared Facilities (SNSF), supported by the National Science Foundation under award ECCS-1542152. K.S. was supported by the Gabilan Stanford Graduate Fellowship and the National Science Foundation Graduate Research Fellowship (DGE-1656518). M.V. was supported by a postdoctoral fellowship from the TomKat Center for Sustainable Energy at Stanford University. F.H. was supported by the Diversifying Academia, Recruiting Excellence (DARE) Doctoral Fellowship Program by Stanford University. J.D. was supported as part of the Department of Energy "Photonics at Thermodynamic Limits" Energy Frontier Research Center under grant DE-SC0019140. **Author contributions:** K.S., M.V., and J.A.D. conceived of the idea and designed the experiments. K.S. performed the experiments with assistance from M.V., A.D., and F.H. K.S. analyzed the data with assistance from M.V. and F.H. D.K.A. led the molecular dynamics simulations. K.S. led the heating simulations with assistance from J.D. J.A.D. supervised the project. K.S. wrote the initial draft and all authors contributed to the final manuscript. **Competing interests:** The authors declare no competing interests. **Data and materials availability:** All data and materials are available upon email request.

SUPPLEMENTARY MATERIALS

science.sciencemag.org/content/371/6526/280/suppl/DC1
Materials and Methods
Supplementary Text
Figs. S1 to S16
Tables S1 and S2
References (*20–27*)
Movie S1

16 June 2020; resubmitted 16 October 2020
Accepted 4 December 2020
10.1126/science.abd2847